

Record-Low and Anisotropic Thermal Conductivity of Quasi-1D Bulk ZrTe₅ Single Crystal

Jie Zhu,^{§,¶,†} Tianli Feng,^{‡,||,†} Scott Mills,[⊥] Peipei Wang,[⊤] Xuewang Wu,[§] Liyuan Zhang,[⊤]
Socrates T. Pantelides,^{‡,||} Xu Du,[⊥] and Xiaojia Wang^{§,*,*}

[§]Department of Mechanical Engineering, University of Minnesota, Minneapolis, MN 55455, USA

[¶]Key Laboratory of Ocean Energy Utilization and Energy Conservation of Ministry of Education, Dalian University of Technology, Dalian, Liaoning 116024, China

[‡]Department of Physics and Astronomy and Department of Electrical Engineering and Computer Science, Vanderbilt University, Nashville, Tennessee 37235, USA

^{||}Materials Science and Technology Division, Oak Ridge National Laboratory, Oak Ridge, Tennessee 37831, USA

[⊥]Department of Physics and Astronomy, Stony Brook University, Stony Brook, New York 11794, USA

[⊤]Department of Physics, Southern University of Science and Technology, Shenzhen, Guangdong 518055, China

^{*}Department of Electrical and Computer Engineering, University of Minnesota, Minneapolis, MN 55455, USA

ABSTRACT

[†] J. Z. and T. L. F. contributed equally to this paper.

^{*}Corresponding author e-mail: wang4940@umn.edu

Zirconium pentatelluride (ZrTe_5) has recently attracted renewed interest owing to many of its newly discovered extraordinary physical properties, such as 2D and 3D topological-insulator behavior, pressure-induced superconductivity, Weyl semimetal behavior, Zeeman splitting, and resistivity anomaly. The quasi-1D structure of single-crystal ZrTe_5 also promises large anisotropy in its thermal properties which have not yet been studied. In this work, via time-domain thermoreflectance measurements, ZrTe_5 single crystals are discovered to possess a record-low thermal conductivity along the b -axis (through-plane), as small as $0.33 \pm 0.03 \text{ W m}^{-1} \text{ K}^{-1}$ at room temperature. This ultralow b -axis thermal conductivity is twelve times smaller than its a -axis thermal conductivity ($4 \pm 1 \text{ W m}^{-1} \text{ K}^{-1}$) owing to the material's asymmetrical crystalline structure. First-principles calculations are further conducted to reveal the physical origins of the ultralow b -axis thermal conductivity, which can be attributed to: 1) the resonant bonding and strong lattice anharmonicity induced by electron lone pairs, 2) the weak interlayer van der Waals interactions, and 3) the heavy mass of Te atoms, which results in low phonon group velocity. This work sheds light on the design and engineering of high-efficiency thermal insulators for applications such as thermal barrier coatings, thermoelectrics, thermal energy storage, and thermal management.

KEYWORDS: *ultra-low thermal conductivity; quasi-1D material; anisotropic thermal transport; time-domain thermoreflectance; first-principles calculation*

1. INTRODUCTION

Recently, ZrTe_5 has drawn increasing attention as a functional material because of its distinct electronic,¹⁻⁶ optical,⁷ and thermal properties⁸⁻¹⁰ such as its resistivity anomaly and good

thermoelectric performance.^{11,12} ZrTe₅ is a layered material stacked along the *b*-axis. Each layer is composed of chains of ZrTe₃ prisms running along the *a*-axis, as shown in Figure 1. These prismatic chains are linked along the *c*-axis via zigzag Te chains to form 2D planes. Therefore, ZrTe₅ is a quasi-one-dimensional (quasi-1D) crystal. The weak van der Waals force between layers makes it easy to mechanically exfoliate thin flakes of ZrTe₅. It has been found that this quasi-1D nature endows ZrTe₅ single crystals with significantly anisotropic electrical conductivity that has promising applications in electronics.^{1,4,5}

Also associated with the quasi-1D nature, the thermal transport properties of ZrTe₅ single crystal may offer intriguing opportunities for applications in the thermal management in electronic devices. To date, the study of thermal transport in ZrTe₅ has been limited to alloys and polycrystals. A few experimental works have reported varying values ranging from 1.5 to 8 W m⁻¹ K⁻¹.^{9,11-13} Most of the values were averaged along different crystalline orientations since the samples were polycrystalline or alloyed.^{11,12} There exists one experimental study of single-crystal ZrTe₅ along the *a*-axis (8 W m⁻¹ K⁻¹).⁹ However, this anomalously high value was considered to have a significant error by other researchers.¹¹ Thus, the anisotropic thermal conductivity of single crystals remains elusive. More importantly, the previously measured values of ZrTe₅ polycrystals and alloys contain substantial electronic contributions and the effects of many unknown defects and grain boundaries on the phononic contribution. Therefore, the intrinsic lattice thermal conductivity of ZrTe₅ may deviate significantly from these reported values. On the other hand, although a few theoretical works have calculated the thermal conductivity of ZrTe₅,^{14,15} the anisotropy has not been studied yet.

In this study, we focus on the anisotropic thermal transport in high-quality, bulk, single-crystal ZrTe₅ along both the basal-plane and through-plane directions. Our approach integrates

theoretical and experimental investigations, revealing the fundamental mechanisms of the anisotropic thermal transport in ZrTe_5 . To achieve this objective, we synthesized large-size high-quality ZrTe_5 crystals and employed the technique of ultrafast time-domain thermoreflectance (TDTR) to study their intrinsic anisotropic three-dimensional (3D) thermal conductivities. We found a record-low thermal conductivity ($0.33 \text{ W m}^{-1} \text{ K}^{-1}$) along the through-plane direction (b axis) of single-crystal ZrTe_5 . To provide physical insights into the experimental work, first-principles calculations have been performed for bulk ZrTe_5 crystals to reveal the characteristics of thermal transport along both the in-plane and through-plane directions. Excellent agreement has been achieved between theoretical and experimental results regarding the thermal conductivities of ZrTe_5 along different crystal orientations. The origin of the poor thermal transport across the ZrTe_5 layers has been revealed by using the theoretical predictions.

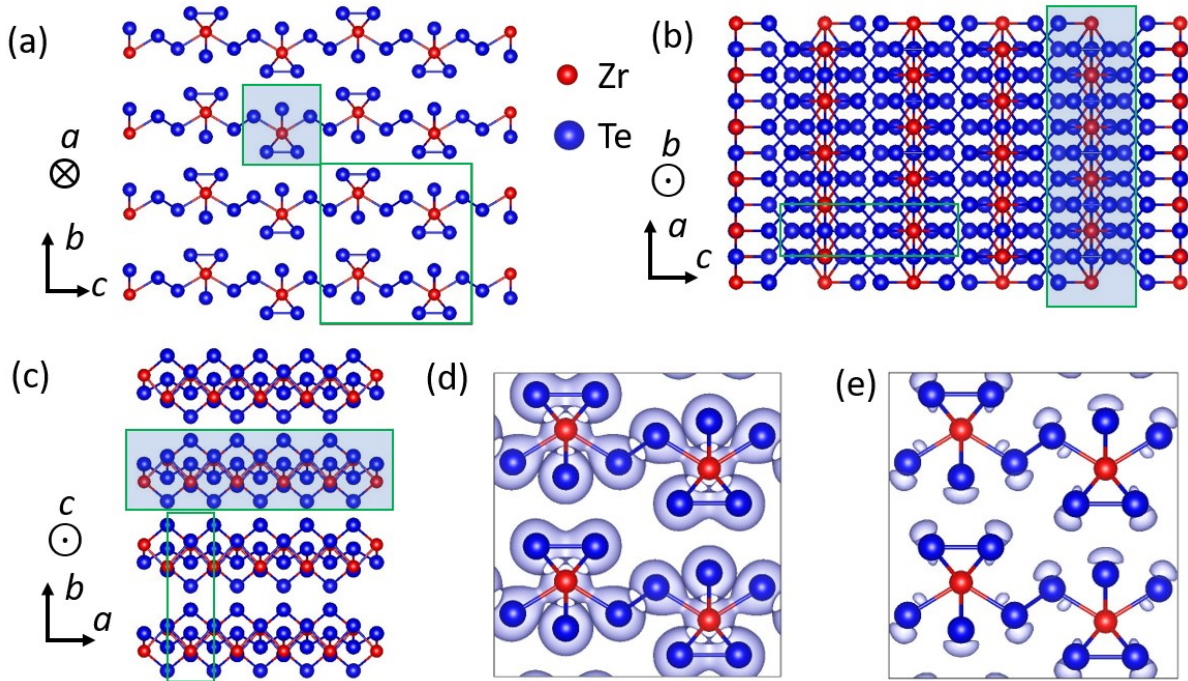


Figure 1. (a,b,c) The lattice structures of ZrTe_5 as viewed against the crystalline a , b , and c axes. The open green boxes indicate unit cells. The shaded green boxes highlight the 1D chains. (d) Electron density and (e) localization function (ELF) isosurfaces at $\text{ELF}=0.88$ calculated using density functional theory.

2. RESULTS

2.1 Structural characterization of ZrTe_5

ZrTe_5 single crystals were synthesized with the chemical vapor transport (CVT) method, which produced ribbon-shaped single crystals with a typical size of $\sim 0.6 \text{ mm} \times 0.6 \text{ mm} \times 5 \text{ mm}$ (Figure 2(a) inset). Figure 2(a) shows the X-ray diffraction spectrum of such a ZrTe_5 crystal, where sharp peaks along the (020) and (080) directions are clearly visible. The quality of the single crystals is better characterized through the temperature dependence of the resistivity along the a -axis as shown in Figure 2(b), where a peak at 140 K is observed, induced by the Lifshitz transition.⁵ The peak position observed here is within the typical range of $T_p = 120 - 150 \text{ K}$ for CVT synthesized high-quality ZrTe_5 single crystals.^{5,16}

2.2 Through-plane thermal conductivity measurements

Three ZrTe_5 flakes have been measured in this work, labeled S-1, S-2, and S-3. For S-1 and S-2 ZrTe_5 flakes, thin transducer films (58 nm and 52 nm, respectively) of aluminum (Al) were deposited for both in-plane and through-plane thermal measurements, while an Al transducer with a typical thickness of 80 nm was coated on sample S-3 for through-plane TDTR experiments only.

In TDTR measurements, a mode-locked Ti:sapphire laser serves as the light source, which produces a train of pulses ($\sim 100 \text{ fs}$) at a repetition rate of 80 MHz. The laser is split into a pump

beam and a probe beam through a polarizing beam splitter. The pump beam is modulated as a sinusoidal wave by an electro-optical modulator (EOM) at a modulation frequency of f_m . A mechanical delay stage varies the optical path of the pump beam, producing a time delay of up to ~ 4 ns between the pump excitation and probe sensing. An objective lens is used to focus both the pump and probe beams on the sample surface with a beam spot size ($1/e^2$ radius) from 3 to 12 microns. The in-phase (V_{in}) and out-of-phase (V_{out}) signals are collected by a photodetector and then an rf lock-in amplifier to the computer for data analysis. The ratio of signals ($-V_{in}/V_{out}$) is compared with a thermal model to extract the unknown thermal properties.¹⁷⁻¹⁹ The Al transducer thickness can be determined simultaneously from picosecond acoustics during TDTR measurements.^{20,21} Figure 2(c) shows a representative picosecond acoustic signal of S-1, and the first echo at 18 ps gives 58 nm as the Al transducer thickness. The acoustic impedance data are detailed in the Supporting Information (SI).

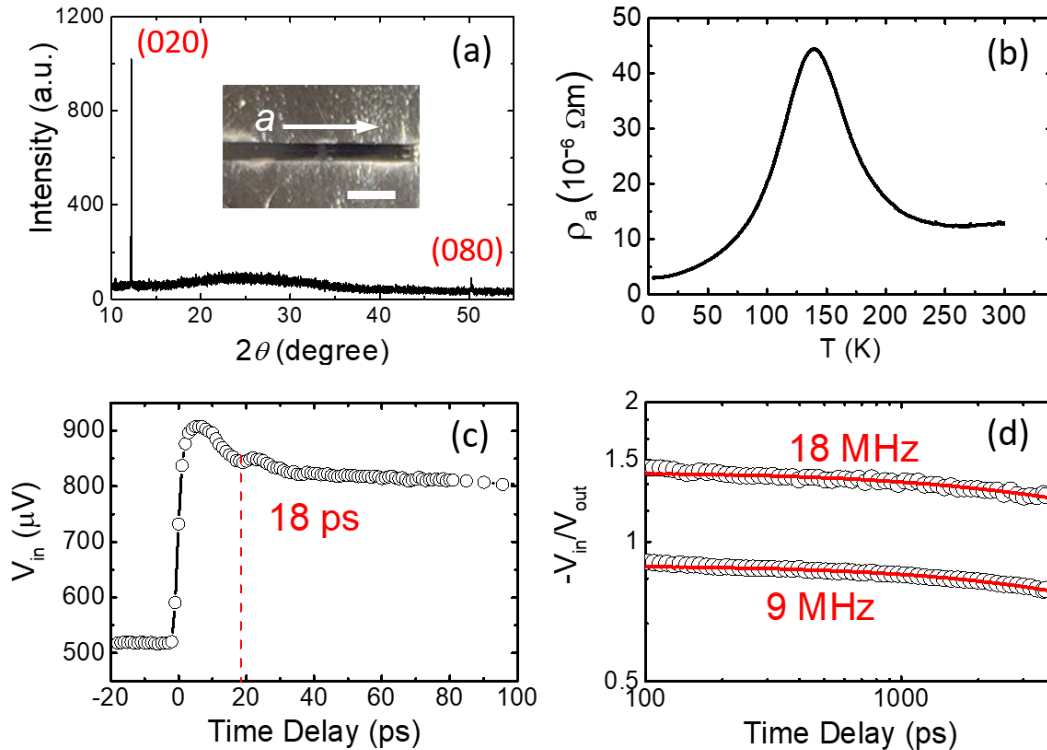


Figure 2. The ZrTe₅ single crystal and through-plane TDTR measurements. (a) XRD data. The inset is a photo image of S-3. The scale bar is 1 mm; (b) The temperature dependence of resistivity along the *a*-axis, where a peak at 140 K is observed, which is induced by the Lifshitz transition; (c) The TDTR in-phase signals for determining Al thickness with picosecond acoustics. The first echo at 18 ps indicates an Al thickness of 58 nm; (d) TDTR ratio signals (open circles) at $f_m = 18$ MHz and 9 MHz with the corresponding best-fit curves (red solid lines).

Multi-frequency through-plane TDTR measurements have been conducted on all three samples.^{22,23} A heat capacity of $1.27 \text{ MJ m}^{-3} \text{ K}^{-1}$ is used for ZrTe₅ crystals in the data analysis.²⁴ The obtained through-plane (along *b* axis) thermal conductivities (Λ_b) are 0.30 ± 0.02 , 0.33 ± 0.03 , and $0.35 \pm 0.03 \text{ W m}^{-1} \text{ K}^{-1}$ for S-1, S-2, and S-3, respectively. The variation among these results for different samples falls within the 8% uncertainty of TDTR measurements, indicating good consistency in the measurements of different samples with varying Al-transducer thicknesses. The averaged Λ_b of $0.33 \pm 0.03 \text{ W m}^{-1} \text{ K}^{-1}$ at room temperature is the record-low thermal conductivity value for single crystals. To date, the experimentally reported lowest thermal conductivity of single-crystal materials in literature is $0.46 \text{ W m}^{-1} \text{ K}^{-1}$, along the *a*-axis of SnSe,²⁵ which was however, partially attributed to the possibly existing porosity of the sample.²⁶ All other single crystals that have been reported to possess low thermal conductivities, *e.g.*, $\beta\text{-Zn}_{13}\text{Sb}_{10}$ ($0.85 \text{ W m}^{-1} \text{ K}^{-1}$)²⁷ and Bi₂Te₃ ($0.76 \text{ W m}^{-1} \text{ K}^{-1}$),²⁸ are all higher than $0.7 \text{ W m}^{-1} \text{ K}^{-1}$.

The representative TDTR signals and fitting curves at modulation frequencies of 18 MHz and 9 MHz for sample S-1 are shown in Figure 2(d). The interfacial thermal conductance between the Al film and ZrTe₅ is within the range of 7 to 11 $\text{MW m}^{-2} \text{ K}^{-1}$ for all three samples, suggesting a relatively weaker interfacial thermal transport between Al and ZrTe₅ than that typically between a metal and a semiconductor. In addition, we took scanning electron

microscope (SEM) images to see the area of the Al/ZrTe₅ interface. We did not see a clear visible contrast at the Al/ZrTe₅ interface in the SEM images (Figure S1 in the SI), which indicates there is no significant Al atom diffusion into ZrTe₅. This is in contrast to previous work showing that metal atoms, such as Pd, can diffuse into ZrTe₅ crystals when they are in contact,⁷ and other metal atoms (*e.g.*, Cu, Ni, Co, or Fe) diffuse into topological insulators (*e.g.*, Bi₂Se₃)²⁹ and thermoelectric materials (*e.g.*, Bi₂Te₃).³⁰

2.3 In-plane thermal conductivity measurements

To obtain the in-plane thermal conductivity of ZrTe₅, we conducted 2D in-plane scanning using the beam-offset approach.³¹⁻³³ During the experiments, the sample was mounted with the *a*-axis along the vertical direction. Figure 3(a) illustrates a CCD image of sample S-2 with a 20× objective lens (beam spot size of ~3 μm), which suggests a sufficiently large and smooth area of the sample surface for the beam-offset measurements.

From a sensitivity analysis detailed in Figure S2 of the SI, we find that the thermal conductivity of the Al transducer has a strong influence on the beam-offset signals. Thus, using accurate thermal properties of the transducer layer for the data analysis is essential to obtain reliable in-plane thermal conductivity of ZrTe₅ in the present experiments. Therefore, prior to the beam-offset measurements of ZrTe₅ samples, we characterized the thermal properties of the Al transducer by measuring the Al/SiO₂ reference samples, which were placed next to the ZrTe₅ samples during the Al sputtering deposition. The thermal properties of Al were obtained from both the through-plane and in-plane TDTR measurements of these reference samples. With a known thermal conductivity of SiO₂ (1.4 W m⁻¹ K⁻¹, as previously verified for the same wafer), we obtained the in-plane thermal conductivity of the Al transducer to be 76 ± 3 W m⁻¹ K⁻¹ as averaged over 3 locations of each sample. This value of Al thin-film transducer is much lower

than that of bulk Al ($237 \text{ W m}^{-1} \text{ K}^{-1}$).³⁴ The volumetric heat capacity of the Al transducer was also determined to be $2.23 \pm 0.04 \text{ MJ m}^{-3} \text{ K}^{-1}$ from through-plane TDTR measurements of the Al/SiO₂ reference samples, which is slightly lower (~9%) than the bulk value ($2.42 \text{ MJ m}^{-3} \text{ K}^{-1}$). These thermal properties of the Al transducer extracted from measurements of reference samples were later used as input parameters in the data analysis of in-plane beam-offset measurements of ZrTe₅, allowing accurate determination of the sample thermal properties as demonstrated in literature.^{33,35}

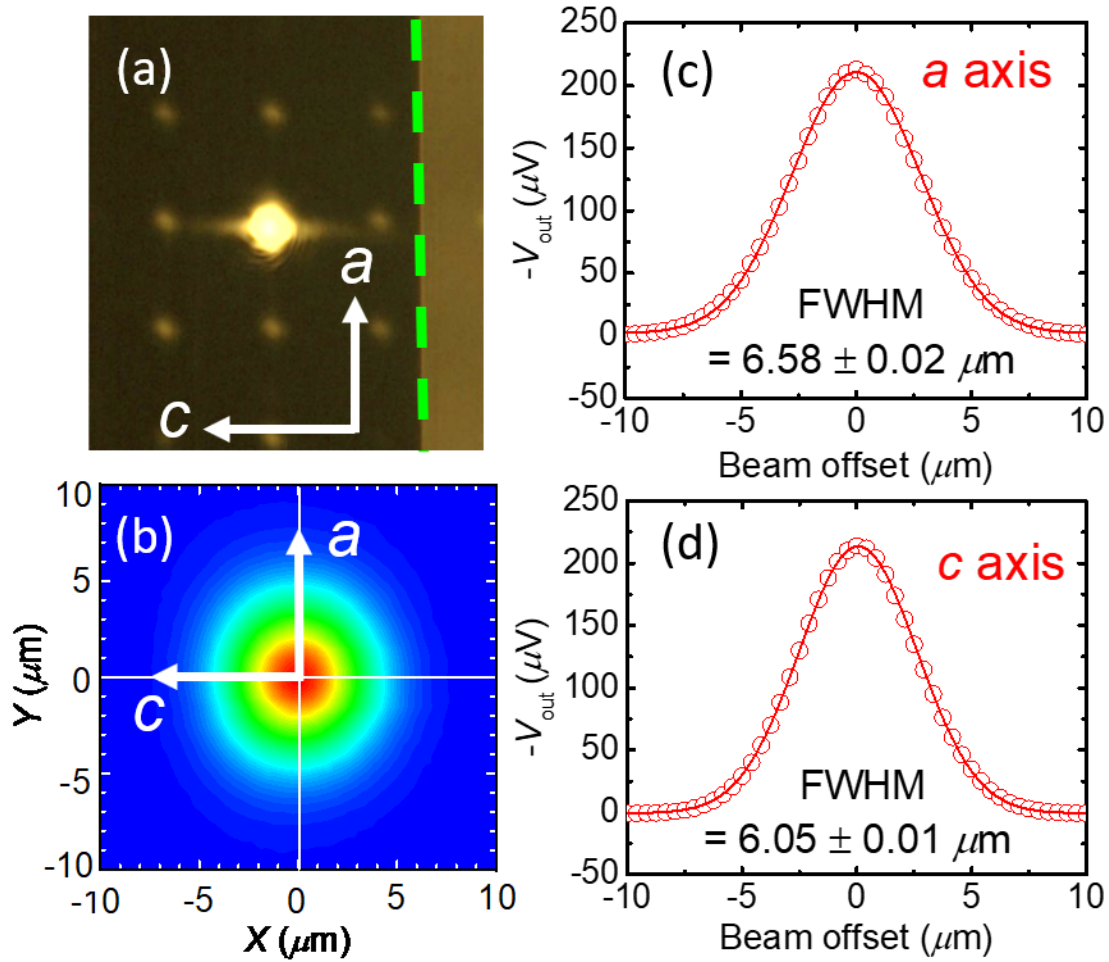


Figure 3. In-plane thermal measurements on ZrTe_5 using the beam-offset method. (a) $20\times$ microscopic CCD image of sample S-2 with a laser beam spot of $\sim 3\ \mu\text{m}$. The a -axis is along the vertical direction and the dashed green line represents the edge of the sample flake; (b) Two-directional beam-offset signal ($-V_{\text{out}}$) contour of sample S-2; (c) and (d) represent the beam-offset signals along the a and c crystal orientations, respectively taken from the 2D contour in (b). The fitting errors in the FWHM are estimated to be less than 0.3%.

The 2D contour plots of the out-of-phase signals (V_{out}) measured by in-plane beam-offset TDTR are illustrated in Figure 3(b) for sample S-2, of which the X axis is along the c -axis of the ZrTe_5 flake. The measurements were conducted at a fixed time delay of -50 ps. Results from this 2D-scanning method generate a contour plot that can be used to extract the in-plane thermal conductivity of ZrTe_5 along any crystalline direction. This method also provides a straightforward manner to accurately determine the primary crystalline directions from post-data processing, eliminating the need to align the sample loading along a certain crystalline orientation for thermal measurements, which can be challenging and time consuming. Corrections on V_{out} mapping signals are made as we detailed in previous work.³³ These corrections are essential for processing the measurement data to obtain accurate thermal properties of the sample.

The in-plane thermal conductivity is obtained by comparing the full width at half maximum (FWHM) of V_{out} along the X or Y directions with the calculated values from the thermal model.^{17,31} Figures 3(c) and (d) show the beam-offset signals along the a and c crystal orientations that are extracted from the 2D contour in Figure 3(b). The in-plane thermal conductivity of ZrTe_5 along the Y direction, which corresponds to the a -axis of sample S-2, is found to be $\Lambda_a = 4.2\ \text{W m}^{-1}\ \text{K}^{-1}$, averaged by 4 measurements on different locations of S-2. An accurate determination of the c -axis thermal conductivity has been prohibited by the poor sensitivity of the beam-offset signals along this direction, presumably due to the lower c -axis

thermal conductivity compared to that along the a -axis. This speculation is consistent with the first-principles calculation results described in Section 3. Using the same approach, we obtain the Λ_a of sample S-1 as $3.8 \text{ W m}^{-1} \text{ K}^{-1}$. Therefore, the averaged $\Lambda_a = 4 \pm 1 \text{ W m}^{-1} \text{ K}^{-1}$, which gives an anisotropy ratio of $\Lambda_a / \Lambda_b \approx 12$ between the a and b axes.

3. THEORETICAL PREDICTIONS

To understand the physical origins of the anisotropic thermal transport and especially the record-low thermal conductivity along the through-plane direction in single-crystal bulk ZrTe_5 , we have performed comprehensive first-principles density functional theory (DFT) calculations.

Our work uses the standard DFT calculations without an extra van der Waals functional. We note that Ref. [14] predicted the thermal conductivities of 8.6, 7.4, $7.2 \text{ W m}^{-1} \text{ K}^{-1}$ for a , b , and c directions by using DFT with an extra vdW functional. Prior studies of the thermal conductivity of vdW crystals such as multilayer graphene, graphite, and Bi_2Te_3 have demonstrated that calculation results from the standard DFT agreed well (or even better) with experimental data, when the vdW functional was excluded.³⁶⁻³⁸ We have examined the relaxed lattice constant from DFT calculations with and without the vdW functional, and we find that they both give reasonable agreement with experiment results (see details in Table S2 of the SI).

The DFT-calculated electron density and localization function are shown in Figures 1(d) and (e), respectively. It is seen that the interlayer gap has weak wavefunction overlap, indicating weak van der Waals interactions. This is consistent with the small through-plane phonon velocity that will be discussed later. The electron localization function profile indicates that electron lone pairs exist in Te atoms so that the bonding between Zr and Te is resonant,³⁹ which can lead to large lattice anharmonicity and low thermal conductivity. This feature will be further confirmed by the strong anharmonic phonon scattering.

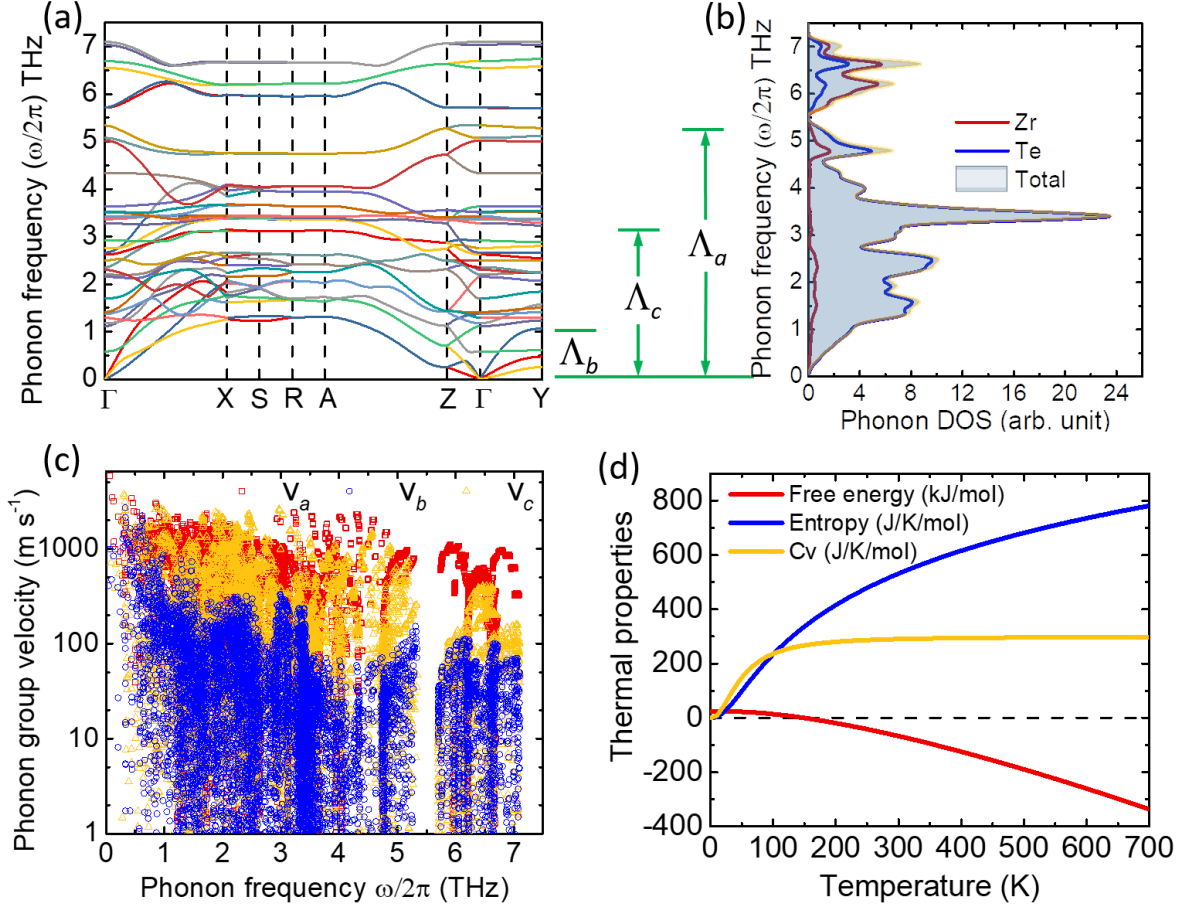


Figure 4. (a) The DFT calculated phonon dispersion relation along high-symmetry directions. (b) The total and projected phonon densities of states. The dominant phonon frequencies for Λ_a , Λ_b , and Λ_c are shown in between (a) and (b). (c) The phonon group velocity spectra along the a , b , and c axes. (d) The heat capacity, entropy, and free energy as functions of temperature.

The DFT-calculated phonon dispersion relation is shown in Figure 4(a). Surprisingly, we find that most of the optical phonon branches along the b -axis ($\Gamma - Y$) are nearly flat, which indicates that their group velocities are nearly 0, *i.e.*, they are almost standing waves and contribute little to direct heat conduction. This result is consistent with the weak van der Waals interlayer interaction observed in the electron density (wave function overlaps) shown in Figure 1(d). We also note that the acoustic phonons along the b -axis ($\Gamma - Y$) have very small group velocities. The calculated total and projected phonon densities of states (DOS) are shown in

Figure 4(b). We find that the Zr and Te atoms have distinct contributions to the lattice vibrations. The Zr atoms predominantly contribute to the high-energy (> 5.5 THz) optical modes due to their lighter atomic mass, while the Te atoms dominate the acoustic phonons as well as all the low-energy optical phonons (< 5.5 THz) due to their large stoichiometric ratio and heavier atomic mass. Such distinct contributions support the observation of resonant bonding, similar to that in PbS^{39,40}. Later, we show that the high-energy (> 5.5 THz) optical modes contribute negligibly to the lattice thermal conductivity, which suggests that the Te atoms dominate the heat conduction while the vibrations of Zr atoms make no substantial contribution to the lattice thermal conductivity.

Figure 4(c) depicts the phonon group velocities (v_g) calculated along the a , b , and c crystalline directions. It can be clearly seen from Figure 4(c) that the phonon group velocities along the b -axis are significantly smaller than those along the c -axis, which are yet smaller than those along the a -axis. These results are consistent with the quasi-1D atomic structure of ZrTe₅, which has the weakest bonding along b and strongest along a . The velocities of the near- Γ acoustic phonons are 2217, 494, and 2185 m s⁻¹, respectively, along $\Gamma-X$, $\Gamma-Y$, and $\Gamma-Z$. The corresponding Debye temperatures calculated by $\Theta_D = (hv_g) / k_B(3n/4\pi)^{(1/3)}$ with n being the atomic density and h being the Plank constant, are 209, 46, and 206 K, respectively, along these three directions. From phonon spectra, thermal properties such as the heat capacity, entropy, and free energy are calculated, as shown in Figure 4(d). From the convergence trend of the temperature-dependent heat capacity, Θ_D of ZrTe₅ is determined to be ~ 150 K, consistent with the average of the values associated with each of the three directions (154 K).

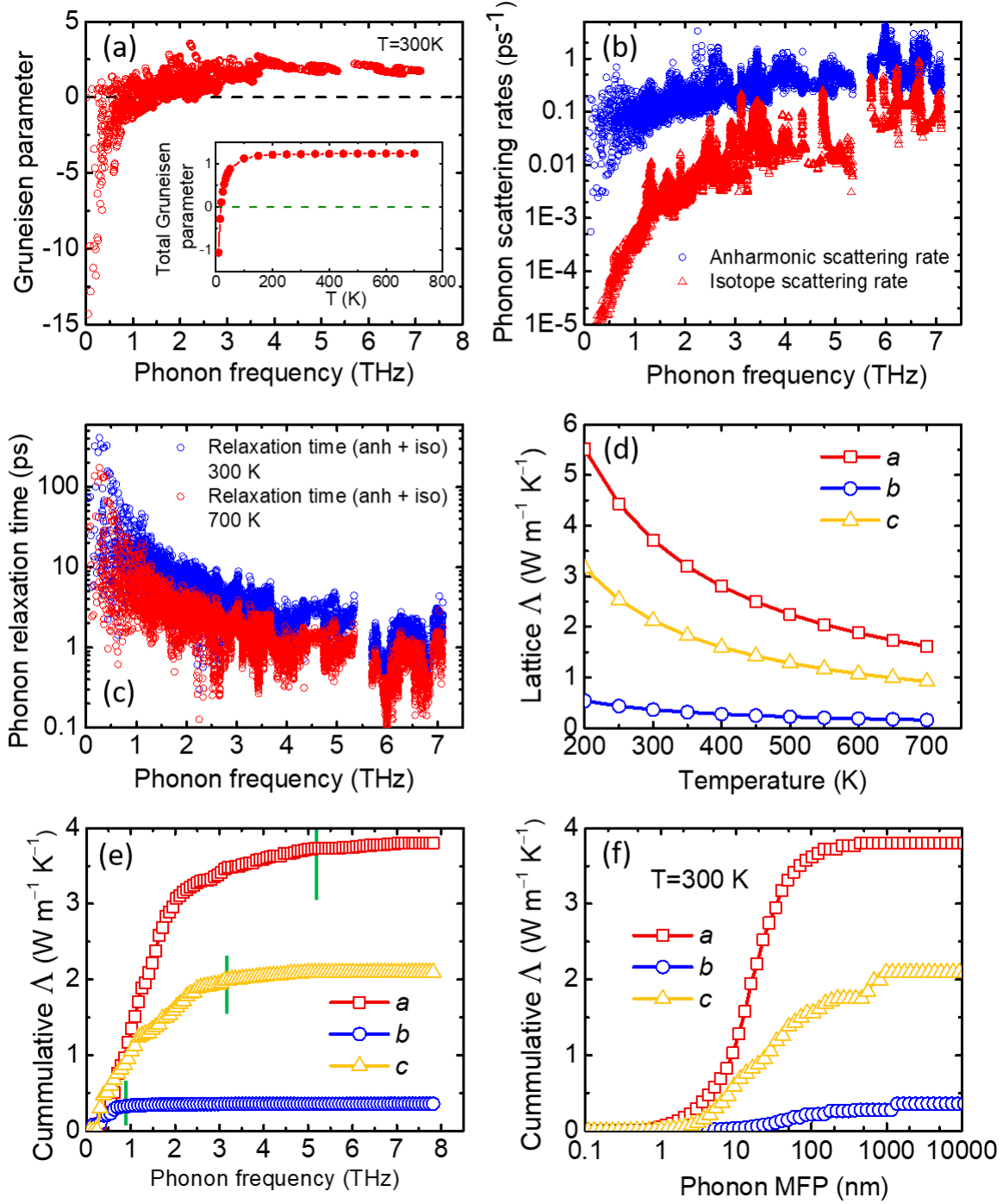


Figure 5. (a) The frequency-dependent room-temperature Grüneisen parameter spectra. The inset shows the temperature-dependent total Grüneisen parameter. (b) frequency-dependent three-phonon and phonon-isotope scattering rates spectra. (c) Phonon relation time spectra at 300 and 700 K. (d) The DFT-calculated temperature-dependent thermal conductivities along the a , b , and c axes. (e,f) Cumulative thermal conductivity as a function of phonon frequency and mean free path.

To gain some insights into the anharmonicity, we calculate the Grüneisen parameter, three-phonon scattering rates, and relaxation times over a range of phonon frequencies, as shown in Figures 5(a), (b) and (c) respectively. The Grüneisen parameter above Θ_D (~ 150 K) converges at 1.25, close to the values of ultra-low-thermal conductivity resonant-bonding materials calculated from DFT in literature, such as SnSe (1.41) and Bi_2Te_3 (1.5).^{25,41} A full comparison is included in Table S1 of the SI. This indicates that the anharmonicity of ZrTe_5 could be very large, which is consistent with what the electron localization function in Figure 1(e) suggests: the electron lone pairs result in resonant bonding and strong anharmonicity. The large three-phonon scattering rates and short relaxation times shown in Figures 5(b) and (c) again support the large anharmonicity.

With these results, we have obtained the room-temperature thermal conductivities (Figure 5(f)) along the a , b , and c directions, which are 3.9, 0.3, and 1.9 $\text{W m}^{-1} \text{K}^{-1}$, respectively, and agree excellently with experimental results. The anisotropy ratio between the a and b axes is as high as 13, while the in-plane anisotropy ratio between the a and c axes is around 2. We also note here that the thermal conductivity along the c -axis is indeed lower than that of the a -axis. This result supports our speculation on why we cannot obtain a certain value along the c -axis through our beam-offset measurements. Further explanations are provided with the sensitivity analysis detailed in Figure S2 of the SI.

To gain some physical interpretation of measurement results, we calculate the cumulative phonon thermal conductivities as functions of phonon frequency and mean free path, which are shown in Figures 5(e) and (f), respectively. It is clearly seen that the thermal conductivities along the a , b , and c directions are contributed by the phonon modes with frequencies (and thus

energies) lower than 1, 3, and 5.5 THz, respectively. The high-energy phonons with frequencies above 5.5 THz do not contribute much to the heat conduction in any direction because they have the shortest relaxation times and small group velocities. Moreover, we have found that the three acoustic branches contribute 43% to the in-plane thermal conductivities (Λ_a and Λ_c), and the 33 optical branches contribute the remaining 57%. In contrast, the three acoustic branches contribute 94% to the through-plane thermal conductivity Λ_b , and the 33 optical branches contribute only the remaining 6%. This result is consistent with the observed nearly-flat dispersion curves shown in Figure 4(a), which indicates standing-wave-like optical phonons that transport little or no energy. The mean-free-path spectra illustrate that the most significant phonons that dominate thermal transport have mean free paths shorter than 100 nm. This information is important for nanoengineering as it provides the guidance to manipulate the most significant phonons. We note that, interestingly, although the through-plane direction has the lowest thermal conductivity, it contains the longest phonon MFP. This behavior has been observed in other van der Waals crystals such as graphite.⁴²

The DFT calculations have allowed us to unveil the physical origins of the ultra-low through-plane thermal conductivity of ZrTe_5 single crystals: 1) the electron lone pairs of Te atoms lead to resonant bonding and strong lattice anharmonicity, 2) the weak interlayer van der Waals interaction leads to slow acoustic phonons and nearly-flat optical phonon branches along the through-plane direction, and 3) the heavy mass of Te leads to low phonon frequencies and small group velocities.

In the following we discuss the comparison between our thermal conductivity and the experimental data in literature. There is only one set of published data available for single-crystal ZrTe_5 thermal measurements,⁹ which however, were questionable as pointed out by Ref. [11] due

to the small size and needlelike shape of the single crystals. For the comparison with polycrystals in literature, there are two simplified ways to average the thermal conductivity, namely, arithmetic $\Lambda = (\Lambda_a + \Lambda_b + \Lambda_c)/3$ and harmonic $1/\Lambda = (1/\Lambda_a + 1/\Lambda_b + 1/\Lambda_c)/3$.⁴³ Using our measured anisotropic thermal conductivity of single-crystal ZrTe₅, the arithmetic average gives $\sim 2 \text{ W m}^{-1} \text{ K}^{-1}$ and the harmonic average gives $0.73 \text{ W m}^{-1} \text{ K}^{-1}$ for polycrystalline ZrTe₅. We consider these to be the upper and lower limits. The thermal conductivity was reported to be $\sim 1.5 \text{ W m}^{-1} \text{ K}^{-1}$ in Ref. [11], which is in between the arithmetic and harmonic averages. Another issue is that for the polycrystalline samples in literature, there might be also bipolar contribution to thermal conductivity. For example, the thermal conductivity of $1.5 \text{ W m}^{-1} \text{ K}^{-1}$ reported in Ref. [11] contains contributions from both lattice and bipolar as suggested by Figure 4(d) of Ref. [11]. If the bipolar contribution is subtracted, the lattice thermal conductivity can be smaller than $1.5 \text{ W m}^{-1} \text{ K}^{-1}$, closer to the lower limit of the harmonic average. Similarly, Ref. [12] measured a thermal conductivity of $\sim 2 \text{ W m}^{-1} \text{ K}^{-1}$ at room temperature with negligible electronic contribution. However, their temperature-dependent thermal conductivity shows an increasing trend, instead of the typical $1/T$ dependence, for room temperature and beyond (Figure 3(a) in Ref. [12]). We suspect it is likely caused by the bipolar contribution as described in Ref. [11].

4. CONCLUSIONS

In summary, we have conducted both experimental and theoretical studies on the anisotropic thermal conductivities of single crystalline ZrTe₅. Three sample flakes were prepared for TDTR thermal measurements. We found that the *b*-axis thermal conductivity of the ZrTe₅ single crystal is as small as $0.33 \pm 0.03 \text{ W m}^{-1} \text{ K}^{-1}$ at room temperature, which is a record-low thermal conductivity values for single crystals. The *a*-axis thermal conductivity is measured as

$4 \pm 1 \text{ W m}^{-1} \text{ K}^{-1}$, giving an anisotropic ratio of $\Lambda_a / \Lambda_b \approx 12$. DFT calculations predict the room-temperature thermal conductivities along a , b and c directions as 3.9, 0.3, and $1.9 \text{ W m}^{-1} \text{ K}^{-1}$, respectively, which agree excellently with experiment results. The physical origins of the ultra-low through-plane thermal conductivity are attributed to: 1) the resonant bonding and strong lattice anharmonicity induced by electron lone pairs of Te atoms, 2) the slow acoustic phonons because of weak interlayer van der Waals interaction, and 3) the low phonon frequencies and group velocities due to the heavy mass of Te. These may shed light on the discovery and construction of ultra-low-thermal conductivity materials for applications such as thermal barrier coating, thermoelectrics, thermal storage, and thermal management.

5. EXPERIMENTAL SECTION

Sample preparation: ZrTe_5 single crystals were synthesized by chemical vapor transport (CVT) method, with iodine as transport agency. Stoichiometric proportions of $\text{Zr}(3\text{N})$ and $\text{Te}(5\text{N})$ powders, together with $5\text{mg ml}^{-1} \text{I}_2$, were loaded into a quartz tube under argon atmosphere. The quartz tube was flame-sealed and then placed in a two-zone furnace, where a temperature gradient from 480°C to 400°C was applied. After 4 weeks reaction, golden, ribbon-shaped single crystals were formed with a typical size of about $0.6 \text{ mm} \times 0.6 \text{ mm} \times 5 \text{ mm}$.

Deposition and Characterization of Al Transducer: In this work, Al films ($\sim 60 \text{ nm}$ thick) were deposited on ZrTe_5 samples by rf sputtering (AJA sputtering system ATC 2200) to serve as metal transducers in TDTR measurements. Small deposition rates ($\leq 1 \text{ nm min}^{-1}$) was used during the sputtering, resulting in lowered thermal conductivity of the Al films. This feature can enhance the beam-offset measurement sensitivity to the in-plane thermal transport. The thickness of the Al transducer was determined from picosecond acoustics of the TDTR in-phase signal,

and the volumetric heat capacity was taken from literature.⁴⁴ To better characterize the transducer, a 300-nm SiO₂ reference sample was also coated with the Al transducer in the same batch with each ZrTe₅ sample. The thermal conductivity and volumetric specific heat of Al were determined from TDTR measurements on the reference SiO₂ sample with known thermophysical properties, as what was done previously.³³

Electrical conductivity measurements: The electrical conductivity measurements were carried out on bulk single crystal ZrTe₅. To enhance the electrical contact, a thin layer of Au was evaporated through a mask onto four isolated spots. Gold wires were then attached to these spots with silver paste, forming the electrodes for standard 4-probe measurements. The sample was cooled down in an Oxford Variable Temperature Insert (VTI). Standard four-terminal resistance measurements were carried out using a lock-in amplifier. The resistivity was then calculated using the measured electrical resistance and the dimensions of the sample device. Due to the small size of our synthesized needlelike ZrTe₅ single crystals, only the resistivity along the *a*-axis was obtained.

Thermal conductivity measurements: In through-plane TDTR measurements, a 5× objective lens was used to focus the pump and probe beams, producing the spot radii that were ~11 to 12 microns. The modulation frequencies were set as 9 MHz and 18 MHz. The final results were averaged using measurements from three different locations. While for the in-plane TDTR measurements, a 20× objective lens was used to produce a much smaller spot radius of ~ 3 μm. In both through-plane and in-plane measurements, the beam spot size was accurately characterized with the beam-offset method at 30-ps delay time to reduce the measurement uncertainty.³³ A delay time of -50 ps and a modulation frequency of 1.6 MHz were used for the in-plane beam-offset thermal measurements.

First-principles calculations: First-principles calculations were carried out with the VASP program package^{45,46} using the projector augmented wave method (PAW)⁴⁶ in the local density approximation (LDA) for exchange-correlation effects. The atoms in the unit cell (composed of two primitive unit cells) were relaxed using a convergence threshold of 10^{-7} eV for the total energy, and 10^{-7} eV Å⁻¹ for the forces on each atom. The plane-wave energy cutoff was 400 eV. The electronic **k**-space integration was performed with the tetrahedron method, involving a 12×6×4 Monkhorst-Pack **k**-mesh. The relaxed lattice constants along *a*, *b*, and *c* were 3.94, 14.26, and 13.53 Å, which fall within a few percent of the experimental values of 3.86-3.99, 14.47-14.53, 13.68-13.72 Å, respectively.^{8,10,47,48} Spin-orbit coupling was not included as it is not critical for lattice vibration properties, and it would extremely increase the computational cost. The lattice constants from experiments as well from different electronic methods in DFT are summarized in Table S2 of the SI. The phonon dispersion was calculated via 3×2×2 unit cells (288 atoms) by the finite displacement method using the PHONOPY package⁴⁹ with a 4×3×2 Monkhorst-Pack **k**-mesh. The thermal conductivity was calculated by the exact solution to the linearized Boltzmann transport equation that is implemented in the ShengBTE package with the detailed formalism and algorithms shown in Ref. [50]. The third-order force constants are calculated by including up to the sixth nearest neighbors. The calculation used a 20×6×6 **q**-mesh. The thermal conductivity convergence with respect to the **q**-mesh is shown in Figure S3 of the SI.

ASSOCIATED CONTENT

The Supporting Information is available free of charge on the ACS Publication website. In the Supporting Information, details regarding the experimental characterization and measurements

are provided, including the impedance calculation, sample microscopic images, and thermal measurement sensitivity analysis. The convergence study and material parameters related to the first-principles calculations are also included.

ACKNOWLEDGEMENTS

This work was supported by the National Science Foundation (NSF) through the University of Minnesota MRSEC under Award Number DMR-1420013 and partially by the Legislative-Citizen Commission on Minnesota Resources and the Institute on the Environment. X.W. thanks the support from NSF (1804840). J.Z. would like to thank the support from the National Natural Science Foundation of China (Grant No. 51336009). Work at Vanderbilt (T.L.F., S.T.P.) was supported in part by Department of Energy grant DE-FG0209ER46554 and by the McMinn Endowment. Computations at Vanderbilt University and ORNL were performed at the National Energy Research Scientific Computing Center (NERSC), a Department of Energy, Office of Science, User Facility funded through Contract No. DE-AC02-05CH11231. Computations also used the Extreme Science and Engineering Discovery Environment (XSEDE). X.D. and L.Z. acknowledge supports from Guangdong Innovative and Entrepreneurial Research Team Program (No.2016ZT06D348) and Shenzhen Fundamental subject research program (JCYJ20170817110751776) and free exploration (JCYJ20170307105434022). X.D. would also like to acknowledge Philip Allen for insightful discussions, and Fernando Camino for the help in characterizing the cross-sections of the ZrTe_5 crystals. This research used resources of the Center for Functional Nanomaterials, which is a US DOE Office of Science Facility, at Brookhaven National Laboratory under Contract No. DE-SC0012704.

References

- (1) Manzoni, G.; Sterzi, A.; Crepaldi, A.; Diego, M.; Cilento, F.; Zacchigna, M.; Bugnon, P.; Berger, H.; Magrez, A.; Grioni, M.; Parmigiani, F. Ultrafast Optical Control of the Electronic Properties of ZrTe₅. *Phys. Rev. Lett.* **2015**, *115* (20), 207402.
- (2) Weng, H.; Dai, X.; Fang, Z. Transition-Metal Pentatelluride ZrTe₅ and HfTe₅: A Paradigm for Large-Gap Quantum Spin Hall Insulators. *Phys. Rev. X* **2014**, *4* (1), 011002.
- (3) Chen, R. Y.; Chen, Z. G.; Song, X. Y.; Schneeloch, J. A.; Gu, G. D.; Wang, F.; Wang, N. L. Magnetoinfrared Spectroscopy of Landau Levels and Zeeman Splitting of Three-Dimensional Massless Dirac Fermions in ZrTe₅. *Phys. Rev. Lett.* **2015**, *115* (17), 176404.
- (4) Li, X. B.; Huang, W. K.; Lv, Y. Y.; Zhang, K. W.; Yang, C. L.; Zhang, B.; Chen, Y. B.; Yao, S. H.; Zhou, J.; Lu, M. H.; Sheng, L.; Li, S. C.; Jia, J. F.; Xue, Q. K.; Chen, Y. F.; Xing, D. Y. Experimental Observation of Topological Edge States at the Surface Step Edge of the Topological Insulator ZrTe₅. *Phys. Rev. Lett.* **2016**, *116* (17), 176803.
- (5) Zhang, Y.; Wang, C.; Yu, L.; Liu, G.; Liang, A.; Huang, J.; Nie, S.; Sun, X.; Zhang, Y.; Shen, B.; Liu, J.; Weng, H.; Zhao, L.; Chen, G.; Jia, X.; Hu, C.; Ding, Y.; Zhao, W.; Gao, Q.; Li, C.; He, S.; Zhao, L.; Zhang, F.; Zhang, S.; Yang, F.; Wang, Z.; Peng, Q.; Dai, X.; Fang, Z.; Xu, Z.; Chen, C.; Zhou, X. J. Electronic Evidence of Temperature-Induced Lifshitz Transition and Topological Nature in ZrTe₅. *Nat. Commun.* **2017**, *8*, 15512.
- (6) Li, Q.; Kharzeev, D. E.; Zhang, C.; Huang, Y.; Pletikosić, I.; Fedorov, A. V.; Zhong, R. D.; Schneeloch, J. A.; Gu, G. D.; Valla, T. Chiral Magnetic Effect in ZrTe₅. *Nat. Phys.* **2016**, *12* (6), 550-554.
- (7) Léonard, F.; Yu, W.; Collins, K. C.; Medlin, D. L.; Sugar, J. D.; Talin, A. A.; Pan, W. Strong Photothermoelectric Response and Contact Reactivity of the Dirac Semimetal ZrTe₅. *ACS Appl. Mater. Interfaces* **2017**, *9* (42), 37041-37047.
- (8) Littleton, R. T., IV; Tritt, T. M.; Kolis, J. W.; Ketchum, D. R. Transition-Metal Pentatellurides as Potential Low-Temperature Thermoelectric Refrigeration Materials. *Phys. Rev. B* **1999**, *60* (19), 13453-457.
- (9) Zawilski, B. M.; Littleton IV, R. T.; Tritt, T. M. Investigation of the Thermal Conductivity of the Mixed Pentatellurides Hf_{1-x}Zr_xTe₅. *Appl. Phys. Lett.* **2000**, *77* (15), 2319-2321.
- (10) Littleton, R. T., IV; Tritt, T. M.; Kolis, J. W.; Ketchum, D. R.; Lowhorn, N. D.; Korzenski, M. B. Suppression of the Resistivity Anomaly and Corresponding Thermopower Behavior in the Pentatelluride System by the Addition of Sb: Hf_{1-x}Zr_xTe_{5-y}Sb_y. *Phys. Rev. B* **2001**, *64* (12), 121104.
- (11) Miller, S. A.; Witting, I.; Aydemir, U.; Peng, L.; Rettie, A. J. E.; Gorai, P.; Chung, D. Y.; Kanatzidis, M. G.; Grayson, M.; Stevanović, V.; Toberer, E. S.; Snyder, G. J. Polycrystalline ZrTe₅ Parametrized as a Narrow-Band-Gap Semiconductor for Thermoelectric Performance. *Phys. Rev. Appl.* **2018**, *9* (1), 014025.

- (12) Hooda, M. K.; Yadav, C. S. Enhanced Thermopower and Low Thermal Conductivity in P-Type Polycrystalline ZrTe₅. *Appl. Phys. Lett.* **2017**, *111* (5), 053902.
- (13) Smontara, A.; Biljaković, K. Thermal Properties of ZrTe₅. *Mol. Cryst. Liq. Cryst.* **1985**, *121*, 141.
- (14) Wang, C.; Wang, H.; Chen, Y. B.; Yao, S.-H.; Zhou, J. First-Principles Study of Lattice Thermal Conductivity in ZrTe₅ and HfTe₅. *J. Appl. Phys.* **2018**, *123*, 175104.
- (15) Gorai, P.; Toberer, E. S.; Stevanović, V. Computational Identification of Promising Thermoelectric Materials among Known Quasi-2D Binary Compounds. *J. Mater. Chem. A*, **2016**, *4*, 11110-11116.
- (16) Lv, Y.-Y.; Zhang, F.; Zhang, B.-B.; Pang, B.; Yao, S.-H.; Chen, Y. B.; Ye, L.; Zhou, J.; Zhang, S.-T.; Chen, Y.-F. Microstructure, Growth Mechanism and Anisotropic Resistivity of Quasi-One-Dimensional ZrTe₅ Crystal. *J. Cryst. Growth* **2017**, *457*, 250-254.
- (17) Cahill, D. G. Analysis of Heat Flow in Layered Structures for Time-Domain Thermoreflectance. *Rev. Sci. Instrum.* **2004**, *75* (12), 5119-5122.
- (18) Zhu, J.; Tang, D. W.; Wang, W.; Liu, J.; Holub, K. W.; Yang, R. G. Ultrafast Thermoreflectance Techniques for Measuring Thermal Conductivity and Interface Thermal Conductance of Thin Films. *J. Appl. Phys.* **2010**, *108* (9), 094315.
- (19) Zhu, J.; Wu, X.; Lattery, D. M.; Zheng, W.; Wang, X. The Ultrafast Laser Pump-Probe Technique for Thermal Characterization of Materials with Micro/Nanostructures. *Nanoscale Microscale Thermophys. Eng.* **2017**, *21* (3), 177-198.
- (20) Eesley, G. L.; Clemens, B. M.; Paddock, C. A. Generation and Detection of Picosecond Acoustic Pulses in Thin Metal Films. *Appl. Phys. Lett.* **1987**, *50* (12), 717-719.
- (21) Thomsen, C.; Grahn, H. T.; Maris, H. J.; Tauc, J. Surface Generation and Detection of Phonons by Picosecond Light Pulses. *Phys. Rev. B* **1986**, *34* (6), 4129.
- (22) Wang, X. J.; Mori, T.; Kuzmych-Ianchuk, I.; Michiue, Y.; Yubuta, K.; Shishido, T.; Grin, Y.; Okada, S.; Cahill, D. G. Thermal Conductivity of Layered Borides: The Effect of Building Defects on the Thermal Conductivity of TmAlB₄ and the Anisotropic Thermal Conductivity of AlB₂. *APL Matter.* **2014**, *2* (4), 046113.
- (23) Zhu, J.; Zhu, Y.; Wu, X. W.; Song, H. L.; Zhang, Y. H.; Wang, X. J. Structure-Thermal Property Correlation of Aligned Silicon Dioxide Nanorod Arrays. *Appl. Phys. Lett.* **2016**, *108* (23), 231903.
- (24) Shaviv, R.; Westrum Jr., E. F.; Fjellvag, H.; Kjekshus, A. ZrTe₅ and HfTe₅: The Heat Capacity and Derived Thermophysical Properties from 6 to 350 K. *J. Solid State Chem.* **1989**, *81* (1), 103-111.

- (25) Zhao, L.-D.; Lo, S.-H.; Zhang, Y.; Sun, H.; Tan, G.; Uher, C.; Wolverton, C.; Dravid, V. P.; Kanatzidis, M. G. Ultralow Thermal Conductivity and High Thermoelectric Figure of Merit in SnSe Crystals. *Nature* **2014**, *508*, 373.
- (26) Wei, P.-C.; Bhattacharya, S.; He, J.; Neeleshwar, S.; Podila, R.; Chen, Y. Y.; Rao, A. M. The Intrinsic Thermal Conductivity of SnSe. *Nature* **2016**, *539*, E1-E2.
- (27) Lo, C.-W. T.; Ortiz, B. R.; Toberer, E. S.; He, A.; Svitlyk, V.; Chernyshov, D.; Kolodiazny, T.; Lidin, S.; Mozharivskyj, Y. Synthesis, Structure, and Thermoelectric Properties of α -Zn₃Sb₂ and Comparison to β -Zn₁₃Sb₁₀. *Chem. Mater.* **2017**, *29* (12), 5249-5258.
- (28) Ainsworth, L. Single Crystal Bismuth Telluride. *Proc. Phys. Soc. B* **1956**, *69* (6), 606-612.
- (29) Walsh, L. A.; Smyth, C. M.; Barton, A. T.; Wang, Q.; Che, Z.; Yue, R.; Kim, J.; Kim, M. J.; Wallace, R. M.; Hinkle, C. L. Interface Chemistry of Contact Metals and Ferromagnets on the Topological Insulator Bi₂Se₃. *J. Phys. Chem. C* **2017**, *121* (42), 23551-23563.
- (30) Cardinal, T.; Devender; Borca-Tasciuc, T.; Ramanath, G. Tailoring Electrical Transport across Metal–Thermoelectric Interfaces Using a Nanomolecular Monolayer. *ACS Appl. Mater. Interfaces* **2016**, *8* (7), 4275-4279.
- (31) Feser, J. P.; Cahill, D. G. Probing Anisotropic Heat Transport Using Time-Domain Thermoreflectance with Offset Laser Spots. *Rev. Sci. Instrum.* **2012**, *83* (10), 104901.
- (32) Feser, J. P.; Liu, J.; Cahill, D. G. Pump-Probe Measurements of the Thermal Conductivity Tensor for Materials Lacking in-Plane Symmetry. *Rev. Sci. Instrum.* **2014**, *85* (10), 104903.
- (33) Zhu, J.; Park, H.; Chen, J. Y.; Gu, X.; Zhang, H.; Karthikeyan, S.; Wendel, N.; Campbell, S. A.; Dawber, M.; Du, X. Revealing the Origins of 3D Anisotropic Thermal Conductivities of Black Phosphorus. *Adv. Electron. Mater.* **2016**, *2* (5), 1600040.
- (34) Moore, J.; McElroy, D.; Barisoni, M. In *Thermal Conductivity Measurements between 78 and 340 K on Aluminum, Iron, Platinum, and Tungsten*, Proc. of the 6th Conference on Thermal Conductivity, 1966; 737-778.
- (35) Liu, J.; Choi, G.-M.; Cahill, D. G. Measurement of the Anisotropic Thermal Conductivity of Molybdenum Disulfide by the Time-Resolved Magneto-Optic Kerr Effect. *J. Appl. Phys.* **2014**, *116* (23), 233107.
- (36) Fugallo, G.; Cepellotti, A.; Paulatto, L.; Lazzeri, M.; Marzari, N.; Mauri, F. Thermal Conductivity of Graphene and Graphite: Collective Excitations and Mean Free Paths. *Nano Lett.* **2014**, *14* (11), 6109-6114.
- (37) Kuang, Y.; Lindsay, L.; Huang, B. Unusual Enhancement in Intrinsic Thermal Conductivity of Multilayer Graphene by Tensile Strains. *Nano Lett.* **2015**, *15* (9), 6121-6127.
- (38) Hellman, O.; Broido, D. A. Phonon Thermal Transport in Bi₂Te₃ from First Principles. *Phys. Rev. B* **2014**, *90* (13), 134309.

- (39) Lee, S.; Esfarjani, K.; Luo, T.; Zhou, J.; Tian, Z.; Chen, G. Resonant Bonding Leads to Low Lattice Thermal Conductivity. *Nat. Commun.* **2014**, *5*, 3525.
- (40) Xu, B.; Feng, T.; Li, Z.; Pantelides, S. T.; Wu, Y. Constructing Highly Porous Thermoelectric Monoliths with High-Performance and Improved Portability from Solution-Synthesized Shape-Controlled Nanocrystals. *Nano Lett.* **2018**, *18* (6), 4034-4039.
- (41) Bessas, D.; Sergueev, I.; Wille, H. C.; Perßon, J.; Ebling, D.; Hermann, R. P. Lattice Dynamics in Bi_2Te_3 and Sb_2Te_3 : Te and Sb Density of Phonon States. *Phys. Rev. B* **2012**, *86* (22), 224301.
- (42) Fu, Q.; Yang, J.; Chen, Y.; Li, D.; Xu, D. Experimental Evidence of Very Long Intrinsic Phonon Mean Free Path Along the C-Axis of Graphite. *Appl. Phys. Lett.* **2015**, *106* (3), 031905.
- (43) Kumar, S.; Singh, R. N. Thermal Conductivity of Polycrystalline Materials. *J. Am. Ceram. Soc.* **1995**, *78* (3), 728-736.
- (44) Ditmars, D. A.; Plint, C. A.; Shukla, R. C. Aluminum. I. Measurement of the Relative Enthalpy from 273 to 929 K and Derivation of Thermodynamic Functions for Al(s) from 0 K to Its Melting Point. *Int. J. Thermophys.* **1985**, *6* (5), 499-515.
- (45) Kresse, G.; Hafner, J. Ab Initio Molecular Dynamics for Liquid Metals. *Phys. Rev. B* **1993**, *47* (1), 558-561.
- (46) Kresse, G.; Furthmüller, J. Efficient Iterative Schemes for Ab Initio Total-Energy Calculations Using a Plane-Wave Basis Set. *Phys. Rev. B* **1996**, *54* (16), 11169-11186.
- (47) Fjellvåg, H.; Kjekshus, A. Structural Properties of ZrTe_5 and HfTe_5 as Seen by Powder Diffraction. *Solid State Commun.* **1986**, *60* (2), 91-93.
- (48) Okada, S.; Sambongi, T.; Ido, M.; Tazuke, Y.; Aoki, R.; Fujita, O. Negative Evidences for Charge/Spin Density Wave in ZrTe_5 . *J. Phys. Soc. Jpn.* **1982**, *51* (2), 460.
- (49) Togo, A.; Oba, F.; Tanaka, I. First-Principles Calculations of the Ferroelastic Transition between Rutile-Type and CaCl_2 -Type SiO_2 at High Pressures. *Phys. Rev. B* **2008**, *78* (13), 134106.
- (50) Li, W.; Carrete, J.; A. Katcho, N.; Mingo, N. Shengbte: A Solver of the Boltzmann Transport Equation for Phonons. *Comput. Phys. Commun.* **2014**, *185* (6), 1747-1758.